Article

Not peer-reviewed version

Extending the Depth of Focus of Infrared Microscope Using a Binary Axicon Fabricated on Barium Fluoride

Molong Han , Daniel Smith , Tauno Kahro , Dominyka Stonyte , Aarne Kasikov , Darius Gailevicius , Vipin Tiwari , Agnes Pristy Ignatius Xavier , Shivasubramanian Gopinath , Soon Hock Ng , Aravind Simon John Francis Rajeswary , Aile Tamm , Kaupo Kukli , Keith Bambery , Jitraporn Vongsvivut , Saulius Juodkazis , Vijayakumar Anand *

Posted Date: 8 March 2024

doi: 10.20944/preprints202403.0471.v1

Keywords: Infrared microscopy; axial resolution; binary axicon; photolithography; femtosecond ablation; chemical imaging doi:10.20944/preprints202403.0471.v1

Article

Extending the Depth of Focus of Infrared Microscope Using a Binary Axicon Fabricated on Barium Fluoride

Molong Han [1], Daniel Smith [1], Tauno Kahro [2], Dominyka Stonytė [3], Aarne Kasikov [2], Darius Gailevičius [3], Vipin Tiwari [2], Agnes Pristy Ignatius Xavier [2,4], Shivasubramanian Gopinath [2], Soon Hock Ng [1], Aravind Simon John Francis Rajeswary [2], Aile Tamm [2], Kaupo Kukli [2], Keith Bambery [5], Jitraporn Vongsvivut [5], Saulius Juodkazis [1,6] and Vijayakumar Anand [1,2]

[1] Optical Sciences Centre and ARC Training Centre in Surface Engineering for Advanced Materials (SEAM), School of Science, Computing and Engineering Technologies, Swinburne University of Technology, Hawthorn, Victoria 3122, Australia; molonghan@swin.edu.au (M.H.); danielsmith@swin.edu.au (D.S.); soonhockng@swin.edu.au (S.H.N.); sjuodkazis@swin.edu.au (S.J.)

[2] Institute of Physics, University of Tartu, 50411 Tartu, Estonia; tauno.kahro@ut.ee (T.K.); aarne.kasikov@ut.ee (A.K.); vipin.tiwari@ut.ee (V.T.); agnes.pristy.ignatius.xavier@ut.ee (A.P.I.X.); shivasubramanian.gopinath@ut.ee (S.G.); aravind@ut.ee (A.S.J.F.R.); aile.tamm@ut.ee (A.T.); kaupo.kukli@ut.ee (K.K.)

[3] Laser Research Center, Physics Faculty, Vilnius University, Sauletekio Ave. 10, 10223 Vilnius, Lithuania; dominyka.stonyte@ff.vu.lt (D.S.); Darius.Gailevicius@ff.vu.lt (D.G.)

[4] School of Electrical and Computer Engineering, Ben Gurion University of the Negev, P.O. Box 653, Beer-Sheva 8410501, Israel

[5] Infrared Microspectroscopy (IRM) Beamline, ANSTO—Australian Synchrotron, Clayton, VIC 3168, Australia; keithb@ansto.gov.au (K.B.); jitrapov@ansto.gov.au (J.V.)

[6] Tokyo Tech World Research Hub Initiative (WRHI), School of Materials and Chemical Technology, Tokyo Institute of Technology, 2-12-1, Ookayama, Meguro-ku, Tokyo 152-8550, Japan

* Correspondence: vijayakumar.anand@ut.ee

Abstract: Axial resolution is one of the most important characteristics of a microscope. In all microscopes, a high axial resolution is desired in order to discriminate information efficiently along the longitudinal direction. However, when studying thick samples that do not contain laterally overlapping information, a low axial resolution is desirable as information from multiple planes can be recorded simultaneously from a single camera shot instead of plane-by-plane mechanical refocusing. In this study, we increased the focal depth of an infrared microscope non-invasively by introducing a binary axicon fabricated on barium fluoride substrate close to the sample. Preliminary results of imaging thick and sparse silk fibers showed an improved focal depth with a slight decrease in lateral resolution and increase in background noise.

Keywords: infrared microscopy; axial resolution; binary axicon; photolithography; femtosecond ablation; chemical imaging

---

1. Introduction

Axial resolving power (ARP), an ability to discriminate information along the longitudinal direction is an important characteristic of all imaging systems [1]. ARP is dependent upon the numerical aperture (NA) and the wavelength λ given as $\sim\lambda/NA^2$. Since the lateral resolving power (LRP), the ability to discriminate information along the transverse direction, is given as $\sim\lambda/NA$, any attempt to change the ARP by changing NA or λ also changes the LRP. While a high LRP – high ARP pair is desirable for most experiments, there are also special cases and scenarios where a high LRP - low ARP pair is desirable. In the case of sparse, thick samples (such as a bunch of fibers and fluorescent samples) the information in one axial plane does not overlap with information in another axial plane laterally. Therefore, if the ARP can be decreased without affecting the LRP, then information from multiple planes can be imaged in a single camera shot [2]. This pair (high LRP- low ARP) can enable rapid imaging of thick and sparse samples.

One imaging solution to achieve the above condition is to implement digital holography techniques [3]. In digital holography technique, only a few camera shots are recorded and the information from multiple planes are reconstructed by numerical back propagation of the recorded holograms or in simple words digital refocusing. Certain digital holography techniques such as Fresnel incoherent correlation holography (FINCH), have naturally surprising LRP-ARP pair [4–7], where their ARP and LRP are lower and higher respectively than those of conventional imaging systems with the same NA. However, digital holography systems are often difficult to implement as they require many optical components and active devices such as spatial light modulators (SLMs) and in most cases require changes in the optical configuration itself. Consequently, it is difficult to implement digital holography techniques such as FINCH in commonly available commercial microscopes.

Another solution to the above problem is to record the microscope's 3D point spread function and use deconvolution methods to reconstruct the object information [8–10]. While deconvolution methods are valuable, the reconstructed images often suffer from reconstruction errors and artifacts. While deep learning methods are now developed to improve the performances of holography systems especially in the reconstruction part, the challenges include obtaining a large data set and time-consuming training processes [11,12]. Computational imaging methods have been developed to tune ARP independent of LRP but require special optical configurations, SLMs and therefore, cannot be used with existing commercial microscopes [13–17].

A well-known, tested solution to achieve the unusual state of high LRP and low ARP is by using an axicon instead of a lens for imaging [18–22]. Axicons generate non-diffracting Bessel beams and therefore have a long focal depth when used for imaging applications [23–32]. In many studies on extending the depth of field using an axicon, the optical configuration has been modified by replacing the lens with an axicon [33], attaching an axicon to a lens [34–36] and in some cases the Bessel beam generated from the axicon was used for illumination of the sample [37,38]. The above modifications are often challenging to implement in an existing commercial microscope. In some cases that use a visible light illumination, a solid axicon may be attached. Still, it may be complicated and impossible in the case of other wavelengths such as infrared (IR), X-rays and Gamma rays.

In this study, we propose and demonstrate an improved optical configuration that allows introducing an axicon close to the object, between the object and the imaging lens for extending the focal depth of an IR microscope. In particular, the initial testing was performed at the Australian Synchrotron facility using a highly intense, highly collimated synchrotron IR beam. The full experiment was carried out in an IR microscope with a Globar™ IR light source at the Australian Synchrotron.

The manuscript consists of ten sections. In the next section, the methodology of extending the depth of focus using an axicon with the object-axicon close to each other is presented. The simulation results of the system are presented in the third section. Optical experiments using a refractive lens and axicon are presented in the fourth section. Optical experiments with a modified configuration using an SLM is presented in the fifth section. The fabrication methods and results are discussed in the sixth section. The initial testing results with synchrotron near IR beam are presented in the seventh section. The results of the final experiments using an internal Globar™ IR light source in a commercial IR microscope are presented in the eighth section. The impact of the method on Synchrotron IR microscope is discussed in the ninth section. The conclusion and future perspectives are presented in the final section.

2. Methods

The optical configuration of a typical microscope with axicon and object close to each other is shown in Figure 1(a). A simplified optical configuration is shown in Figure 1(b) for theoretical analysis. In this study, only spatially incoherent illumination is considered and so the theoretical calculation is performed for an object point and directly extended to a complicated object. Let us consider an object point emitting light with an amplitude of $\sqrt{I_s}$. The light from this object point is incident on a thin axicon located at a distance of z_{s1} with a phase function given as $exp(-i2\pi\Lambda^{-1}R)$, where Λ is the period of the modulo-2π structure and $R = (x^2 + y^2)^{1/2}$. The complex amplitude after the axicon is given as $\sqrt{I_s}C_1L\left(\frac{\bar{r}_s}{z_{s1}}\right)Q\left(\frac{1}{z_{s1}}\right)exp(-i2\pi\Lambda^{-1}R)$, where $Q(b) = exp(i\pi b\lambda^{-1}R^2)$ is a quadratic phase function, $L\left(\frac{\bar{s}}{z_{s1}}\right) = exp\left[i2\pi(\lambda z_{s1})^{-1}(s_x x + s_y y)\right]$ is a linear phase function and C_1 is a complex constant. In general, when a plane wave is incident on the thin axicon, a Bessel beam J_0 is generated. The complex amplitude reaching a refractive lens with a phase of $exp[-i\pi(\lambda f)^{-1}R^2]$ located at a distance of z_{s2} from the axicon is given as $\sqrt{I_s}C_1L\left(\frac{\bar{r}_s}{z_{s1}}\right)Q\left(\frac{1}{z_{s1}}\right)exp(-i2\pi\Lambda^{-1}R)\otimes Q\left(\frac{1}{z_{s2}}\right)$, where '$\otimes$' is a 2D convolutional operator. The complex amplitude after the lens is given as $\left\{\sqrt{I_s}C_1L\left(\frac{\bar{r}_s}{z_{s1}}\right)Q\left(\frac{1}{z_{s1}}\right)exp(-i2\pi\Lambda^{-1}R)\otimes Q\left(\frac{1}{z_{s2}}\right)\right\}exp\{-i\pi(\lambda f)^{-1}R^2\}$ and the intensity distribution at the image sensor located at a distance of z_h from the lens is given as $I_{PSF} = \left|\left\{\sqrt{I_s}C_1L\left(\frac{\bar{r}_s}{z_{s1}}\right)Q\left(\frac{1}{z_{s1}}\right)exp(-i2\pi\Lambda^{-1}R)\otimes Q\left(\frac{1}{z_{s2}}\right)\right\}exp\{-i\pi(\lambda f)^{-1}R^2\}\otimes Q\left(\frac{1}{z_h}\right)\right|^2$. The intensity for an object O is given as $I_O = I_{PSF}\otimes O$. For a single object point, the complex amplitude $\sqrt{I_s}C_1L\left(\frac{\bar{r}_s}{z_{s1}}\right)Q\left(\frac{1}{z_{s1}}\right)exp(-i2\pi\Lambda^{-1}R)$ generates a magnified Bessel intensity distribution J_0 at a distance of z depending on the strength of the quadratic phase function. Now, the rest of the optical set up only reimages the Bessel distribution J_0 with a transverse magnification given as z_h/z_{s2} and longitudinal magnification of $(z_h/z_{s2})^2$ assuming z_{s1} is negligible. This reimaging processing reorganizes the Bessel intensity distribution close to the lens with the far-field ring pattern matched with the image plane. In other words, in the image plane, a ring pattern is obtained for a point object in the object plane and therefore it is necessary to set the distance z_h such that it is not matched with the image plane of the system but at a shorter distance where the Bessel intensity distribution or line focus is obtained. It must be noted that within the imaging depth, the magnification of image can vary depending upon the distances z_{s1}, z_{s2} and z_h. For instance, when a thin object is imaged, the object appears with different sizes within the image depth due to one-many object-image mapping of axicon instead of the usual one-one mapping in a lens.

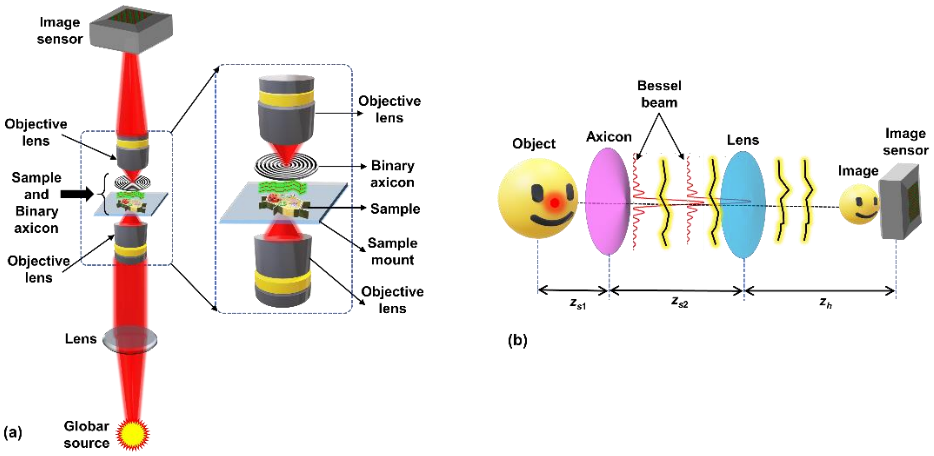

Figure 1. (a) Optical configuration of microscope with object and axicon close to each other. (b) Simplified optical configuration for analysis.

Therefore, it is possible to obtain a Bessel beam even with a commercial microscope with intact objective lenses by introducing an axicon and slightly disturbing the imaging condition. Based on spatially incoherent imaging, every object point is mapped to a Bessel intensity distribution and there is intensity addition in the regions of overlap of Bessel beams generated for two different object points.

3. Simulation Studies

A simulation study was carried out in MATLAB with a matrix size of 500 × 500 pixels, pixel size Δ = 10 μm and wavelength λ = 650 nm. For comparison between a regular microscope and the modified microscope with an axicon close to the object, the distances were selected as $z_s = z_{s1} + z_{s2} = 1$ m, where $z_{s1} = 0.2$ m and $z_{s2} = 0.8$ m and $z_h = 1$ m and the focal length of the refractive lens is $f = 0.5$ m to achieve 2f configuration and a transverse and longitudinal magnifications $M_T = 1$ and $M_L = 1$. Now two objects: ring object with a diameter of 1 mm and a line object with a length of 2 mm and both with a thickness of 10 μm were simulated at distances $z_s = 1$ m and $z_s = 0.8$ m respectively. The simulated I_{PSF}s corresponding to the two locations $z_s = 1$ and $z_s = 0.8$ m for regular microscope and microscope with an axicon are shown in Figure 2(a)-2(d) respectively. The imaging results of the two-plane object using a regular microscope and microscope with an axicon when focusing on the two planes $z_s = 1$ and $z_s = 0.8$ m are shown in Figure 2(e)-2(f) respectively. As it is seen from the results, with an axicon, the depth of focus of a regular microscope is improved with an additional background noise arising due to the sidelobes of the Bessel distribution. The only drawback in the case of microscope with an axicon is the loss or suppression of some higher spatial frequencies due to the sidelobes of the Bessel function and additional background noise.

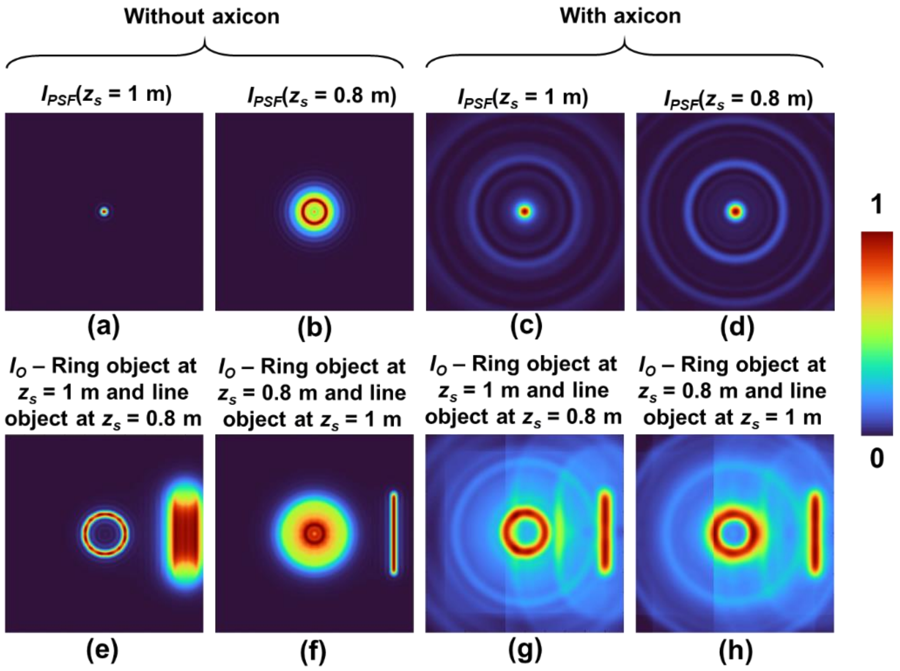

Figure 2. Simulated I_{PSF}s (a) $z_s = 1$ m and (b) $z_s = 0.8$ m for a regular microscope and (c) $z_s = 1$ m and (d) $z_s = 0.8$ m for a microscope with an axicon. Simulated imaging outcomes for regular microscope when (e) ring object is in focus, (f) line object is in focus. Simulated imaging outcomes for microscope with an axicon when (g) ring object is in focus and (h) line object is in focus.

4. Optical Experiments with a Solid Axicon

An optical experiment was carried out using a solid axicon with a base angle of 2.5 degrees and a refractive lens with a focal length $f = 3.5$ cm in a 2f configuration. The axicon was mounted close to the object. The object digit '4' (Group – 0, Element – 4) from USAF resolution target (Thorlabs, R3L3S1N negative target) was illuminated with a blue LED (λ = 450 nm and $\Delta\lambda$ = 18 nm) using a refractive lens. The image was recorded using an image sensor (Zelux CS165MU/M 1.6 MP monochrome CMOS camera, 1440×1080 pixels with pixel size ~3.5 μm). Two recordings were made at two different planes separated by a distance of 1 cm one without an axicon and one with an axicon. The images of the object recorded with an axicon at planes 1 and 2 are shown in Figure 3(a) and 3(b) respectively. The images of the object recorded without an axicon at planes 1 and 2 are shown in

Figures 3(c) and 3(d) respectively. In the cases of recordings in the presence of an axicon, the object information at both planes are simultaneously focused with additional background noise. In the two cases without axicon, the object information when imaging condition is satisfied appear focused whereas the object information when imaging condition is disturbed by 1 cm, appear blurred as expected. There are three effects when an axicon is introduced into an imaging system. (1) Within the focal depth of the axicon, the image appears focused but can be magnified depending upon the distance. (2) The sidelobes of the Bessel function suppresses some of the higher spatial frequencies resulting in a slight blur in the recorded images. (3) The other non-central intensity maxima of the Bessel distribution cause a background effect.

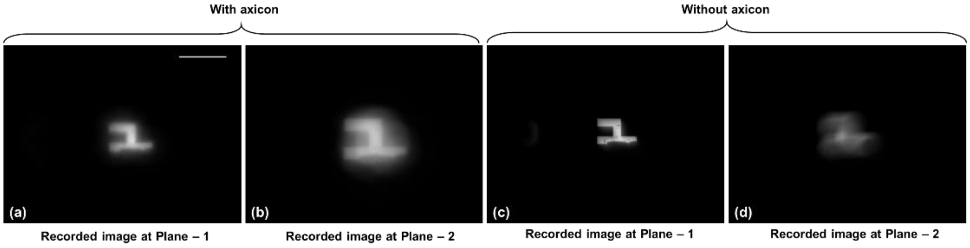

Figure 3. Imaging results with axicon (a) plane 1 and (b) plane 2. Imaging results without axicon for (c) plane 1 and (d) plane 2. Scale bar 1 mm.

5. Optical Experiments with a Spatial Light Modulator

A modified optical experiment of multiplane imaging was carried out using an SLM in a setup as shown in Figure 4. In this study, the phase of diffractive axicon was combined with the phase of a diffractive lens and the imaging was carried out in the near field. The setup consists of high-power green LED from Thorlabs (λ = 554 nm and 650 mW), iris, diffuser (Thorlabs Ø1″ Ground Glass Diffuser-220 GRIT), polarizer, refractive lenses (f = 5 cm), object (Group 3 - digits '1' and '4' from Thorlabs R1DS1N-Negative 1951 USAF Test Target), beam splitter, SLM (Thorlabs Exulus HD2, 1920×1200 pixels, pixel size = 8 μm), band pass filter (Thorlabs FLH532-4, λ = 532 nm and $\Delta\lambda$ = 4 nm) and an image sensor (Zelux CS165MU/M 1.6 MP monochrome CMOS camera, 1440×1080 pixels with pixel size ~3.5 μm). The light from the LED enters the diffuser through an iris and is collected using the refractive lens 1. The diffuser is used here to remove the grating lines and other noises from the LED. The collimated light from the refractive lens 1 enters the polarizer oriented along the active axis of the SLM. The object is critically illuminated by the refractive lens 2 and the light from the object is collimated by refractive lens 3. The collimated light enters the beam splitter and reaches the SLM. On the SLM, phase masks were displayed and the holograms were captured by the image sensor placed at a distance z_h = 17.8 cm. A bandpass filter was used to improve the visibility of the recordings. The test objects namely digits '1' and '4' were mounted at different depths z_s = 5 cm and z_s = 5.1 cm respectively and recorded. The phase mask of a diffractive lens (f = 17.8 cm) and the phase mask obtained by modulo-2π phase addition of phase of a diffractive lens (f = 50 cm) and a diffractive axicon (Λ = 200 μm) are shown in Figures 5(a) and 5(b) respectively. The direct image when both objects are at the same depth is shown in Figure 5(c). The optical imaging results for diffractive lens and diffractive lens-diffractive axicon are shown in Figures 5(d) and 5(e) respectively. In case of diffractive lens, the object '1' is focused and object '4' is blurred. But in the case of diffractive lens-diffractive axicon, both objects '1' and '4' are in focus.

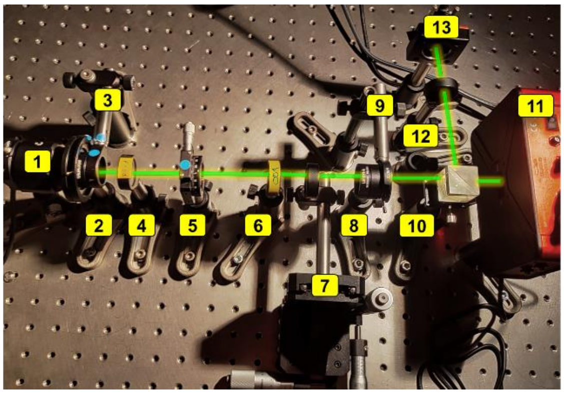

Figure 4. Snapshot of optical experimental setup: (1) high power green LED, (2) iris, (3) diffuser, (4) refractive lens 1, (5) polarizer, (6) refractive lens 2, (7) object, (8) refractive lens 3, (9) iris, (10) beam splitter, (11) SLM, (12) band pass filter, (13) image sensor. The green line shows the beam path from LED to image sensor.

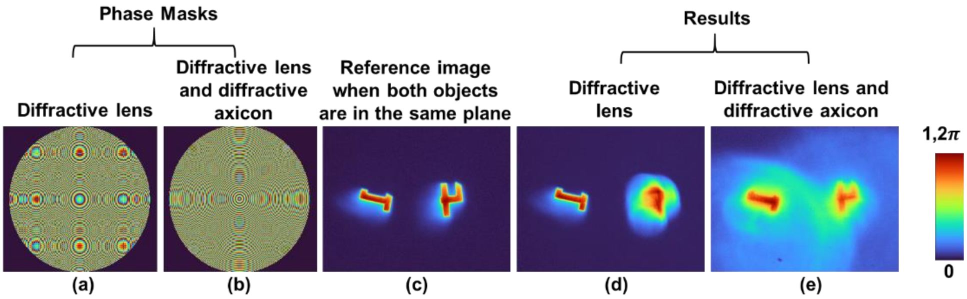

Figure 5. Phase masks of (a) diffractive lens, (b) combination of diffractive axicon and diffractive lens. (c) Image recorded with both objects digit '1' and '4' in the same plane. (d) and (e) Images recorded with (a) and (b) respectively.

6. Fabrication of Binary Axicon

Two binary axicons were manufactured on barium fluoride (BaF_2) substrates (Crystran, United Kingdom) with a diameter of an inch and thickness of 1 mm using two different methods namely photolithography and femtosecond ablation as an amplitude and phase element respectively. The maximum diffraction efficiencies for amplitude and binary phase elements are 10% and 40% respectively, in the first diffraction order [39,40]. The BaF_2 substrates unlike glass substrates are brittle and can be easily damaged. The design for photolithography was made in MATLAB and the image file was converted into lithography file format GDSII using LinkCAD software. To limit the memory of the file size, the sampling size was set to a low value which resulted in pixelated rings.

The first binary axicon was manufactured with a period $\Lambda = 100$ μm using photolithography technique in an ISO5 clean-room. The entire fabrication procedure in two major steps are shown in Figure 6. The positive photoresist (AR-P 3510T, Allresist, Germany) was spin coated (4000 rpm, 60 s) with a thickness of 2 μm onto BaF_2 substrates and then softly baked on a hot plate at 100 °C for 60 s. The promoter AR 300-80 (15-30nm) (Allresist, Germany) was used to improve the adhesion between the photoresist and the BaF_2 substrates. Maskless Aligner (Heidelberg Instruments μMLA, Germany) with a dose control of the light source at 390 nm was used to expose the photoresist, AR 300-44 (Allresist, Germany) was used for developing the UV irradiated structures and ultrapure water was used to remove possible residuals.

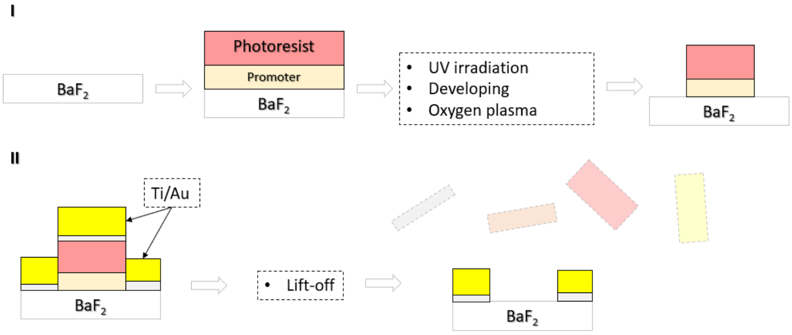

Figure 6. Fabrication procedure of binary axicon using photolithography.

Before metallization, the surface of BaF$_2$ was treated with oxygen plasma. Thereafter, Ti and Au (the thicknesses approximately 6 nm and 100 nm, respectively) was electron beam evaporated at room temperature in a process vacuum of about 2×10^{-6} mbar with a growth rate of ~2 Å/s. A Thin Ti layer was used to improve the adhesion between Au and the glass. Finally, the lift-off procedure was carried out in ultrasonic bath filled with warm acetone to remove excess metal and photoresist. The optical microscope image of the binary axicon and the magnified central area are shown in Figure 7(a) and 7(b) respectively.

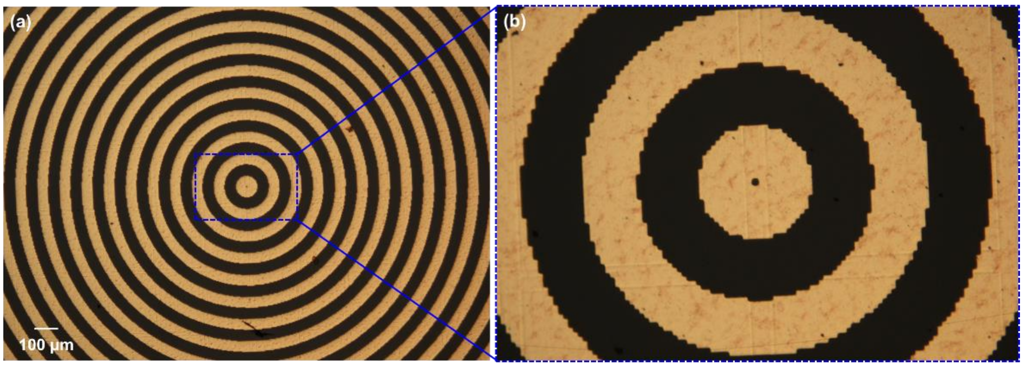

Figure 7. (a) Optical microscope image of the binary axicon and (b) its magnified central part manufactured using photolithography.

The second binary axicon was manufactured using femtosecond ablation with a period $\Lambda = 50$ μm. The sample was fabricated using a femtosecond pulsed direct laser write approach. The fundamental harmonic (1030 nm) of an ultrashort pulsed solid-state Yb:KGW laser system (Pharos, Light Conversion) was directed to an external harmonic generator (HIRO, Light Conversion) where the beam was converted to a 4th harmonic (257 nm). Laser was working at a repetition rate of 100 kHz generating 240 fs duration pulses. The pulse energy was set to 1.21 μJ and the beam was focused on a sample using a Thorlabs LMU-10X-UVB objective with NA = 0.24. The incident beam diameter (at 1/e^2 intensity level) was measured using a CCD camera (Spiricon SP503U, Ophir) and was 2\ω_0 = 4.6 mm. The sample was scanned on precise translation stages (Aerotech ANT 180) at a linear velocity of 500 μm/s. The optical microscope image of the binary axicon is shown in Figure 8(a). The measured 3D surface topography is shown in Figure 8(b) and the extracted 2D profiles reveal a depth of~6.4 μm. This value gives an expected maximum efficiency of 40% at λ = ~5 μm with a refractive index of BaF$_2$ is 1.4. The fabrication duration for a single device was 5 hrs. It must be noted that the above two fabrication techniques were used as they were available and there are different fabrication methods for manufacturing a binary axicon which can be used [41–43].

doi:10.20944/preprints202403.0471.v1

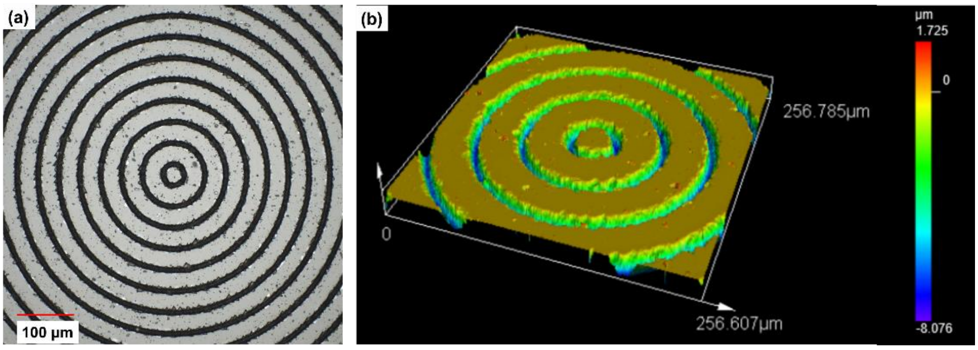

Figure 8. (a) Optical microscope image of the binary axicon and (b) surface profile of the binary axicon fabricated using femtosecond ablation.

7. Experiments with Synchrotron IR Beam

The fabricated devices were tested with the synchrotron IR beam using an optical configuration as shown in Figure 9 similar to a recently demonstrated phase imaging concept [44]. The IRM beamline at the Australian Synchrotron consists of two IR microscopes, one with Globar™ IR source and one with synchrotron IR beam with a high brightness. In particular, the fabricated binary axicons were tested with synchrotron near IR beam using a high-resolution camera Canon EOS 6D (5568 × 3708) pixels with a pixel pitch of 6.5 µm and a high sensitivity to near IR (NIR) wavelengths. The camera was used without the imaging lenses attached. The synchrotron NIR beam is extracted using a NIR window which blocks all the IR wavelengths except for those in the NIR spectral range. The synchrotron IR beam has a unique fork shaped intensity distribution which makes implementing unconventional imaging techniques such as digital holography and coded aperture imaging a challenging task [10,45]. A pinhole was used to extract a uniform circular region from the fork shaped beam which underwent diffraction and an Airy diffraction pattern was obtained. The binary axicons were mounted in this plane of Airy pattern and the intensity distribution of the Bessel beam was recorded. The images of the Bessel distributions obtained for the amplitude-type binary axicon and phase-only binary axicon are shown in Figure 9.

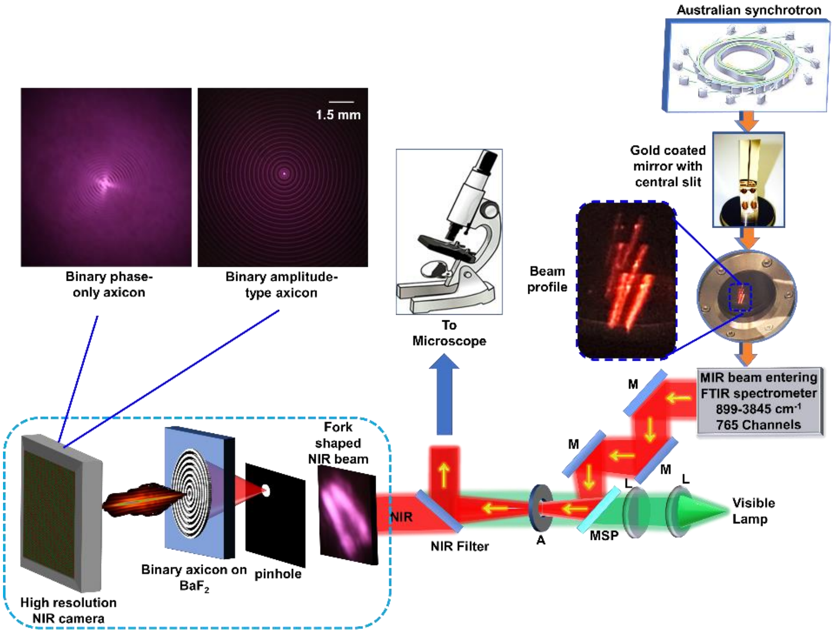

Figure 9. Optical configuration for testing the amplitude-type and phase-only binary axicons with synchrotron NIR beam.

8. Experiments with IR Microscope

To demonstrate imaging of multiple planes, a thick but sparse sample such as a bunch of silk fiber was selected and mounted on the standard sample mounting plane. Two cases were recorded and compared, including one without and one with the binary axicon. For the final demonstration, only the phase-only binary axicon was selected due to the low power illumination from the internal Globar™ IR source. However, if the IR source has a high brightness, both phase-only and amplitude-type binary axicons can be used. The images were captured using a liquid nitrogen cooled 64×64 element focal point array (FPA) Mercury-Cadmium-Telluride detector. The image capturing and processing was controlled by OPUS v.8.0 software (Bruker Optik GmbH, Ettlingen, Germany). The Figure 10(a) shows the visible image of the silk sample that was first recorded using the visible camera equipped in the IR microscope. Two IR chemical images were subsequently collected using the FPA imaging detector on the same location with and without an axicon as presented in Figures 10(b) and 10(c) respectively. The images were obtained by selecting the narrow absorption band of silk sample shown in Figure 10(c) followed by an integration of the information in that spectral region. By comparison, the results clearly reveal an improved focal depth in the image taken with the axicon compared to without axicon. The IR absorption spectrum of the silk sample is shown in Figure 10(d) with characteristic IR peaks of the silk within MIR spectral region. It is worth noting that there is an additional background noise and a slightly lower resolution when imaging with an axicon due to the sidelobes and non-central intensity maxima of the Bessel distribution. The sample is illuminated using a broadband IR region 899-3845 cm^{-1} which correspond to ~2.5-12 μm. As seen from the characterization results in Figure 8 and diffraction efficiency dependency on thickness, the optimal efficiency of 40% can be obtained at ~5 μm and the efficiency decreases at other wavelengths [39,40]. The absorption peak of the silk sample is around 6.2 μm and therefore has a reasonable efficiency of ~35%.

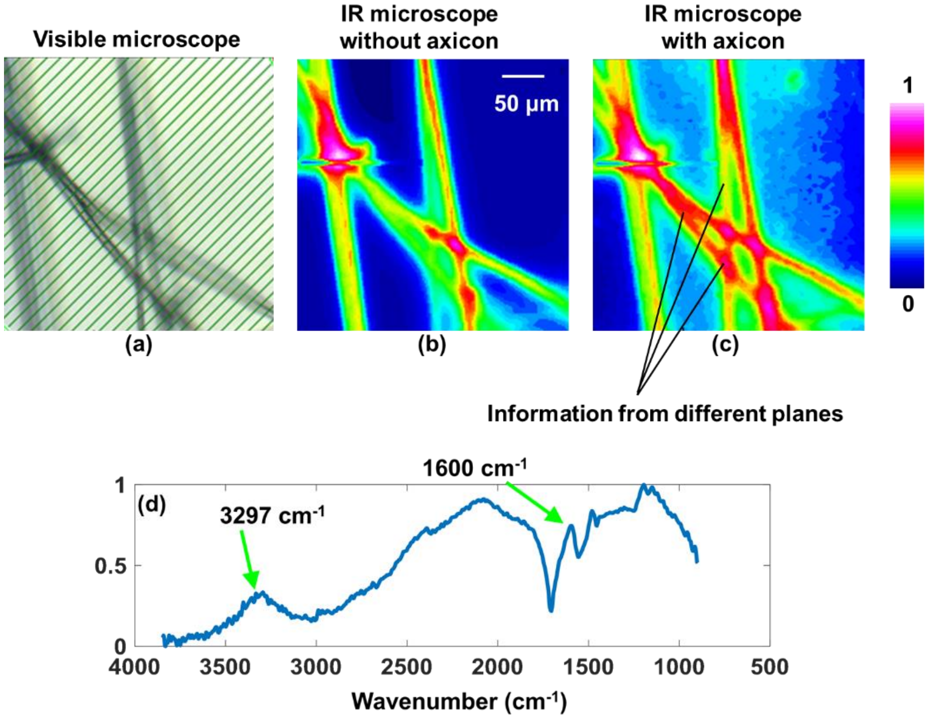

Figure 10. a) Reference visible image of silk sample with white light. (b) Chemical images of silk sample taken without and (c) with a binary axicon. (d) Normalized IR absorption spectrum of silk sample.

9. Discussion

Most synchrotron facilities tend to be unique in their capabilities and feature finite access times for various users. In this particular case, the Australian Synchrotron has a state-of-the-art IR microspectroscopy system with two illumination sources namely the Globar™ IR source and synchrotron IR beam. The microspectroscopy system with synchrotron IR beam is essentially the most used system for high resolution chemical imaging of a diverse range of samples from many research disciplines with a high demand beamtime grants limited to a maximum of approximately 1600 hours tri-annually. The IR imaging study of thick samples layer by layer is a valuable, yet time-consuming procedure that is either overlooked or skipped due to the limitation of the access and period of available beamtimes. The developed and demonstrated idea with a binary axicon reported in this study possesses a strong potential to enable a rapid and routine analysis for a wide range of thick and sparse samples.

10. Conclusion and Future Perspectives

Extending the focal depth of imaging systems using axicons is currently a tested method, but numerous configurations have been demonstrated in the past for different applications. In this study, we present a non-invasive approach to extend the focal depth of an IR microscope using binary axicons manufactured on BaF_2 substrates. Simulation and experimental studies with both visible and IR wavelengths have been carried out.

The idea is that when axicons are used with lenses, there are both spherical and conical phases in play [46–52]. Depending upon the distances and configurations, it is possible to access the near or far fields. The spherical phase either compresses or stretches the Bessel distribution of the conical phase axially depending on the cumulative effects of the phases of the lenses and propagation distances. In the near field, a Bessel distribution is obtained which is the region of interest for extending the focal depth. In the far-field, for every object point, a focused ring pattern is generated, where the focusing effect can be attributed to the spherical phase. Multiple optical experiments with visible light have been demonstrated.

The final experiment has been carried out in the IR microscope of the Australian Synchrotron with an internal Globar™ IR source. The preliminary results are promising as multiple planes of the test object have been successfully imaged in a single shot. We believe that the developed method and device will benefit the ongoing research and development for the users of the Australian Synchrotron's IR beamline, as well as other synchrotron IR facilities. In the future, greyscale axicon with a high diffraction efficiency will be manufactured on BaF_2. Research on suppressing the sidelobes and background and achieving needle beams will enable imaging thicker samples with sparse distributions rapidly.

Author Contributions: Conceptualization, V. A.; S. J.; D. G.; A. T.; K. K.; J. V.; and K. B.; methodology, V. A.; S. J.; D. G.; A. T.; K. K.; J. V.; S. H. N.; and K. B.; Synchrotron experiments, M. H.; D. S.; V. A.; K. B.; and J. V.; Photolithography, T. K.; K. K.; A. T.; Femtosecond fabrication, D. St.; D. G.; Optical experiments, S. G.; V. T.; A. P. I. X.; A. S. J. F. R.; and V. A.; investigation, All authors; resources, V. A.; S. J.; D. G.; A. T.; K. K.; J. V.; and K. B; writing—original draft preparation, All the authors; writing—review and editing, All the authors; supervision, V. A.; S. J.; D. G.; A. T.; K. K.; J. V.; S. H. N.; project administration, V. A.; S. J.; A. T.; K. K.; and J. V.; funding acquisition, V. A.; S. J.; D. G.; A. T.; K. K.; T. K.; S. G.; S. H. N.; M. H.; All authors have read and agreed to the published version of the manuscript.

Funding: The research was funded by European Union's Horizon 2020 Research and Innovation Programme grant agreement No. 857627 (CIPHR) and DP240103231 from the Australian Research Council. This research was undertaken on the IRM beamline at the Australian Synchrotron (Victoria, Australia), part of ANSTO (Proposal ID. 20635, Reference No. AS233/IRM/20635). The research was conducted using the NAMUR+ core facility funded by the Estonian Research Council (TT 13).

Data Availability Statement: Data are available from the authors upon reasonable request.

Conflicts of Interest: The authors declare no conflicts of interest.

References

1. Mertz, J. *Introduction to Optical Microscopy*, 2nd ed.; Cambridge University Press: Cambridge, UK, 2019.
2. Park, S.; Kang, W.; Kwon, Y.D.; Shim, J.; Kim, S.; Kaang, B.K.; Hohng, S. Superresolution fluorescence microscopy for 3D reconstruction of thick samples. *Mol. Brain* **2018**, *11*, 17.
3. Tahara, T.; Quan, X.Y.; Otani, R.; Takaki, Y.; Matoba, O. Digital holography and its multidimensional imaging applications: A review. *Microscopy* **2018**, *67*, 55–67.
4. Rosen, J.; Brooker, G. Digital spatially incoherent Fresnel holography. *Opt. Lett.* **2007**, *32*, 912–914.
5. Brooker, G.; Siegel, N.; Wang, V.; Rosen, J. Optimal resolution in Fresnel incoherent correlation holographic fluorescence microscopy. *Opt. Express* **2011**, *19*, 5047–5062.
6. Rosen, J.; Brooker, G. Non-scanning motionless fluorescence three-dimensional holographic microscopy. *Nat. Photon.* **2008**, *2*, 190–195.
7. Rosen, J.; Alford, S.; Anand, V.; Art, J.; Bouchal, P.; Bouchal, Z.; Erdenebat, M.-U.; Huang, L.; Ishii, A.; Juodkazis, S.; et al. Roadmap on Recent Progress in FINCH Technology. *J. Imaging* **2021**, *7*, 197.
8. Praveen, P.A.; Arockiaraj, F.G.; Gopinath, S.; Smith, D.; Kahro, T.; Valdma, S.-M.; Bleahu, A.; Ng, S.H.; Reddy, A.N.K.; Katkus, T.; et al. Deep Deconvolution of Object Information Modulated by a Refractive Lens Using Lucy-Richardson-Rosen Algorithm. *Photonics* **2022**, *9*, 625.
9. Anand, V.; Han, M.; Maksimovic, J.; Ng, S.H.; Katkus, T.; Klein, A.; Bambery, K.; Tobin, M.J.; Vongsvivut, J.; Juodkazis, S.; et al. Single-shot mid-infrared incoherent holography using Lucy-Richardson-Rosen algorithm. *Opto-Electron. Sci.* **2022**, *1*, 210006.
10. Ng, S.H.; Anand, V.; Han, M.; Smith, D.; Maksimovic, J.; Katkus, T.; Klein, A.; Bambery, K.; Tobin, M.J.; Vongsvivut, J.; et al. Computational Imaging at the Infrared Beamline of the Australian Synchrotron Using the Lucy–Richardson–Rosen Algorithm. *Appl. Sci.* **2023**, *13*, 12948.
11. Wang, et. al. Unsupervised Deep Learning Enables 3D Imaging for Single-Shot Incoherent Holography. *Laser Photonics Rev*. **2024**, 2301091.
12. Shimobaba, T.; Blinder, D.; Birnbaum, T.; Hoshi, I.; Shiomi, H.; Schelkens, P.; Ito, T. Deep-Learning Computational Holography: A Review (Invited). *Front. Phys.* **2022**, *3*, 854391.
13. Anand, V. Tuning Axial Resolution Independent of Lateral Resolution in a Computational Imaging System Using Bessel Speckles. *Micromachines* **2022**, *13*, 1347.
14. Kumar, R.; Vijayakumar, A.; Rosen, J. 3D single shot lensless incoherent optical imaging using coded phase aperture system with point response of scattered airy beams. *Sci. Rep.* **2023**, *13*, 2996.
15. Bleahu, A.; Gopinath, S.; Kahro, T.; Angamuthu, P.P.; Rajeswary, A.S.J.F.; Prabhakar, S.; Kumar, R.; Salla, G.R.; Singh, R.P.; Kukli, K.; et al. 3D Incoherent Imaging Using an Ensemble of Sparse Self-Rotating Beams. *Opt. Express* **2023**, *31*, 26120–26134.
16. Gopinath, S.; Rajeswary, A.S.J.F.; Anand, V. Sculpting axial characteristics of incoherent imagers by hybridization methods. *Opt. Lasers Eng.* **2024**, *172*, 107837.
17. Gopinath, S.; Anand, V. Post-Ensemble Generation with Airy Beams for Spatial and Spectral Switching in Incoherent Imaging. *Preprint* 111910, Opticaopen. https://doi.org/10.1364/opticaopen.25273810
18. McLeod, J. The Axicon: A new type of optical element. *J. Opt. Soc. Am.* **1954**, *44*, 592–597.
19. Durnin, J. Exact solutions for nondiffracting beams. I. The scalar theory. *J. Opt. Soc. Am. A* **1987**, *4*, 651–654.
20. Durnin, J.; Miceli, J.J., Jr.; Eberly, J.H. Diffraction-free beams. *Phys. Rev. Lett.* **1987**, *58*, 1499.
21. Lapointe, M.R. Review on non-diffracting Bessel beam experiments. *Opt. Laser Technol.* **1992**, *24*, 315–321.
22. Khonina, S.N.; Kazanskiy, N.L.; Karpeev, S.V.; Butt, M.A. Bessel Beam: Significance and Applications—A Progressive Review. *Micromachines* **2020**, *11*, 997.
23. Khonina, S.N.; Karpeev, S.; Alferov, S.; Savelyev, D.; Laukkanen, J.; Turunen, J. Experimental demonstration of the generation of the longitudinal E-field components on the optical axis with high-numerical-aperture binary axicons illuminated by linearly and circularly polarized beams. *J. Opt.* **2013**, *15*, 085704.
24. Khonina, S.N.; Degtyarev, S. A longitudinally polarized beam generated by a binary axicon. *J. Russ. Laser Res.* **2015**, *36*, 151–161.
25. Khonina, S.N.; Kotlyar, V.; Soifer, V.; Jefimovs, K.; Paakkonen, P.; Turunen, J. Astigmatic Bessel laser beams. *J. Mod. Opt.* **2004**, *51*, 677–686.
26. Khonina, S.; Kotlyar, V.; Skidanov, R.; Soifer, V.; Jefimovs, K.; Simonen, J.; Turunen, J. Rotation of microparticles with Bessel beams generated by diffractive elements. *J. Mod. Opt.* **2004**, *51*, 2167–2184.

27. Khonina, S.N.; Kazanskiy, N.L.; Khorin, P.A.; Butt, M.A. Modern Types of Axicons: New Functions and Applications. *Sensors* **2021**, *21*, 6690.
28. Arimoto, R.; Saloma, C.; Tanaka, T.; Kawata, S. Imaging properties of axicon in a scanning optical system. *Appl. Opt.* **1992**, *31*, 6653–6657.
29. Bouchal, P.; Kapitan, J.; Konecny, M.; Zboncak, M.; Bouchai, Z. Non-diffracting light in nature: Anomalously reflected self-healing Bessel beams from jewel scarabs. *APL Photonics* **2019**, *4*, 126102.
30. Schafer, F.P. On some properties of axicons. *Appl. Phys. B* **1986**, *39*, 1–8.
31. Scott, G.; McArdle, N. Efficient generation of nearly diffraction-free beams using an axicon. *Opt. Eng.* **1992**, *31*, 2640–2643.
32. Vasara, A.; Turunen, J.; Friberg, A.T. Realization of general nondiffracting beams with computer-generated holograms. *JOSA A* **1989**, *6*, 1748–1754.
33. Dufour, P.; Piche, M.; Koninck Y.; D.; McCarthy, N. Two-photon excitation fluorescence microscopy with a high depth of field using an axicon. *Appl. Opt*. **2006**, *45*, 9246-9252.
34. Snoeyink, C.; Wereley, S. Single-image far-field subdiffraction limit imaging with axicon. *Opt. Lett*. **2013**, *38*, 625-627.
35. Schreiber, B.; Elsayad, K.; Heinze, K.G. Axicon-based Bessel beams for flat-field illumination in total internal reflection fluorescence microscopy. *Opt. Lett.* **2017**, *42*, 3880–3883.
36. Theriault, G.; Koninck, Y.D.; McCarthy, N. Extended depth of field microscopy for rapid volumetric two-photon imaging. *Opt. Express* **2013**, *21*, 10095–10104.
37. Sheppard, C.J.R.; Castello, M.; Tortarolo, G.; Deguchi, T.; Koho, S.V.; Vicidomini, G.; Diaspro, A. Image scanning microscopy with multiphoton excitation or Bessel beam illumination. *J. Opt. Soc. Am. A* **2020**, *37*, 1639–1649.
38. Perinchery, S.M.; Haridas, A.; Shinde, A.; Buchnev, O.; Murukeshan, V.M. Breaking diffraction limit of far-field imaging via structured illumination Bessel beam microscope (SIBM). *Opt. Express* **2019**, *27*, 6068–6082.
39. Soifer, V.A. (Ed.) *Computer Design of Diffractive Optics*, 1st ed.; Woodhead Publishing: Cambridge, UK, 2012.
40. O'Shea, D.C.; Suleski, T.J.; Kathman, A.D.; Prather, D.W. *Diffractive Optics: Design, Fabrication, and Test*; SPIE Press: Bellingham, WA, USA, 2004; Volume 62.
41. Watt, F.; Bettiol, A.A.; Kan, J.A.V.; Teo, E.J.; Breese, M.B.H. Ion beam lithography and nanofabrication: A review. *Int. J. Nanosci.* **2005**, *4*, 269–286.
42. Chou, S.Y.; Krauss, P.R.; Renstrom, P.J. Nanoimprint lithography. *J. Vac. Sci. Technol. B* **1996**, *14*, 4129–4133.
43. Tseng, A.A.; Chen, K.; Chen, C.D.; Ma, K.J. Electron beam lithography in nanoscale fabrication: Recent development. *IEEE Trans. Electron. Packag.* **2003**, *26*, 141–149.
44. Han, M.; Smith, D.; Ng, S.H.; Katkus, T.; John Francis Rajeswary, A.S.; Praveen, P.A.; Bambery, K.R.; Tobin, M.J.; Vongsvivut, J.; Juodkazis, S.; et al. Single shot lensless interferenceless phase imaging of biochemical samples using synchrotron near infrared Beam. *Biosensors* **2022**, *12*, 1073.
45. Anand, V.; Ng, S.H.; Katkus, T.; Maksimovic, J.; Klein, A.; Vongsvivut, J.; Bambery, K.; Tobin, M.J.; Juodkazis, S.; Exploiting spatio-spectral aberrations for rapid synchrotron infrared imaging. *J. Synchrotron. Rad.* **2021**, *28*, 1616-1619.
46. Burvall, A.; Kołacz, K.; Jaroszewicz, Z.; Friberg, A.T. Simple lens axicon. *Appl. Opt.* **2004**, *43*, 4838–4844.
47. Belanger, P.; Rioux, M. Ring pattern of a lens-axicon doublet illuminated by a Guassian beam. *Appl. Opt.* **1978**, *17*, 1080–1088.
48. Jaroszewicz, Z.; Morales, J. Lens axicons: systems composed of a diverging aberrated lens and a perfect converging lens. *JOSA* **1998**, *15*, 2383-2390.
49. Rajesh, K. B.; Suresh, V. N.; Anbarasan, P. M.; Gokulakrishnan, K.; Mahadevan, G. Tight focusing of double ring shaped radially polarized beam with high NA lens axicon. *Opt. Laser Technol*. **2011**, *43*, 1037-1040.
50. Khonina, S.N.; Volotovsky, S.G.; Ustinov, A.V.; Porfirev, A.P. Spatiotemporal dynamics of the polarisation state of laser radiation performed by lens-axicon combinations. *Phys. Lett. A* **2019**, *383*, 2535–2541.

51. Takanezawa, S.; Saitou, T.; Imamura, T. Wide field light-sheet microscopy with lens-axicon controlled two-photon Bessel beam illumination. *Nat. Commun.* **2021**, *12*, 2979.
52. Bhuian, B.; Winfield, R.J.; O'Brien, S.; Crean, G.M. Pattern generation using axicon lens beam shaping in two-photon polymerization. *Appl. Surf. Sci.* **2007**, *254*, 841–844.